ROYAL SOCIETY
OF CHEMISTRY

EDGE ARTICLE

Check for updates

Partial thermal atomization of residual Ni NPs in single-walled carbon nanotubes for efficient CO_2 electroreduction†

Fengwei Zhang, [ID] ‡*[a] Han Zhang,‡[a] Yang Zhao,[b] Jingjing Li,[c] Chong Guan,[a] Jijie Li,[a] Xuran Wang,[a] Yuewen Mu, [ID] [a] Wen-Yan Zan [ID] *[a] and Sheng Zhu [ID] *[ad]

CO_2 electroreduction (CO_2RR) is an important solution for converting inert CO_2 into high value-added fuels and chemicals under mild conditions. The decisive factor lies in the rational design and preparation of cost-effective and high-performance electrocatalysts. Herein, we first prepare a novel f-SWNTs-650 catalyst *via* a facile partial thermal atomization strategy, where the residual Ni particles in single-walled carbon nanotubes (SWNTs) are partially converted into atomically dispersed NiN_4 species. CO_2RR results show that the competitive evolution hydrogen reaction (HER) predominates on pristine SWNTs, while f-SWNTs-650 switches the CO_2 reduction product to CO, achieving a CO faradaic efficiency (FE_{CO}) of 97.9% and a CO partial current density (j_{CO}) of -15.6 mA cm^{-2} at -0.92 V *vs.* RHE. Moreover, FE_{CO} is higher than 95% and j_{CO} remains at -10.0 mA cm^{-2} at -0.82 V *vs.* RHE after 48 h potentiostatic electrolysis. Combined with systematic characterization and density functional theory (DFT) calculations, the superior catalytic performance of f-SWNTs-650 is attributed to the synergistic effect between the NiN_4 sites and adjacent Ni NPs, that is, Ni NPs inject electrons into NiN_4 sites to form electron-enriched Ni centers and reduce the energy barrier for CO_2 activation to generate the rate-limiting *COOH intermediate, thus implementing the efficient electroreduction of CO_2.

1. Introduction

The massive emission of CO_2 based on fossil fuels has caused increasingly serious energy crises and environmental issues,[1–4] and the desire to make full use of renewable energy to realize carbon neutrality is growing.[5–7] The electrochemical CO_2 reduction reaction (CO_2RR) is considered as a promising approach for recycling CO_2 and storing intermittent renewable electricity.[8–10] However, the chemical inertness of CO_2 molecules (806 kJ mol^{-1}),[11] competitive hydrogen evolution reaction (HER), and multiple reaction pathways of up to 16 possible

[a]*Institute of Crystalline Materials, Institute of Molecular Science, Key Lab of Materials for Energy Conversion and Storage of Shanxi Province, Key Laboratory of Chemical Biology and Molecular Engineering of Education Ministry, Shanxi University, Taiyuan 030006, P. R. China. E-mail: fwzhang@sxu.edu.cn; zanwy@sxu.edu.cn; shengzhu@sxu.edu.cn*

[b]*Dalian National Laboratory for Clean Energy, Dalian Institute of Chemical Physics, Chinese Academy of Sciences, Dalian 116023, Liaoning, P. R. China*

[c]*Address Research Institute of Resource-based Economy Transformation and Development, Shanxi University of Finance and Economics, Taiyuan 030006, P. R. China*

[d]*Institute for Carbon-Based Thin Film Electronics, Peking University, Shanxi (ICTFE-PKU), Taiyuan 030012, P. R. China*

† Electronic supplementary information (ESI) available. See DOI: https://doi.org/10.1039/d4sc07291j

‡ These authors contributed equally to this work.

products result in low energy efficiency during the electrocatalytic conversion process.[12–14] To tackle these problems, significant efforts have been made to develop earth-abundant transition metal single-atom electrocatalysts, facilitating the CO_2RR to give an attractive CO feedstock for important chemical reactions such as downstream hydroformylation,[15] carbonylation and Fischer–Tropsch synthesis.[16] Although atomically dispersed M–N–C catalysts (M = Fe, Co, Ni, *etc.*) with MN_x moieties have shown great potential for directing the CO_2RR to CO,[17,18] the majority of them are currently prepared by pyrolysis of metal salts coordinated with heteroatomic compounds, uneconomical metal–organic frameworks and covalent-organic framework materials.[19,20] The complicated fabrication procedure and the inevitable high-temperature annealing ($\geq$900 °C) for acquiring satisfactory conductivity often lead to low-quality electrocatalysts with elusive structures being affected by metal aggregation.[21] Thus, designing and developing highly efficient and robust non-noble metal-based electrocatalysts is significant to the practical utilization of renewable energy for the CO_2RR.

Single-walled carbon nanotubes (SWNTs) have been extensively used in fields such as semiconductors, biomedicine, electronics and energy storage due to their high specific surface area,[22] excellent conductivity,[23] biocompatibility and mechanical behavior.[24] As a significant synthetic method, arc discharge has long been used to prepare high quality SWNTs, typically

with nickel-based catalysts.[25] Nevertheless, there is a large amount of residual Ni nanoparticles (NPs) in SWNT skeletons, and researchers usually purify SWNTs by removing Ni NPs under harsh acid conditions. Unfortunately, acid etching not only fails to completely remove the firmly encapsulated Ni NPs but also disrupts the structure of SWNTs,[26] posing huge challenges for subsequent practical application. To solve this problem, abandoning the idea of deliberately removing residual Ni NPs, we here first report the synthesis of a novel f-SWNTs-650 catalyst. Specifically, polyformamide decorated SWNTs (PFA@SWNTs) were obtained *via in situ* formamide self-condensation followed by mild heat treatment in a flowing Ar atmosphere. Interestingly, this process favored partial transformation of residual Ni NPs into a large number of atomically dispersed Ni sites on the surface of SWNTs due to the thermal atomization. X-ray absorption fine structure spectra (XAFS) and extended XAFS spectra (EXAFS) prove that Ni single atoms are present in the form of NiN_4 configuration. CO_2RR results show that the FE_{CO} is 97.9% and the partial current density of CO (j_{CO}) is -15.6 mA cm^{-2} at -0.92 V *vs.* RHE for the f-SWNTs-650 catalyst, which are significantly higher than those of pristine SWNTs (0.7%, -0.04 mA cm^{-2}). Potentiostatic electrolysis at -0.82 V *vs.* RHE maintained a FE_{CO} of 95.0% and a j_{CO} of -10.0 mA cm^{-2} for 48 h showing the long-term stability of the f-SWNTs-650 catalyst. Detailed characterization combined with DFT calculations proves that the presence of Ni NPs significantly enhances the CO_2 activation ability of the f-SWNTs-650 catalyst by injecting electrons into the NiN_4 center through the carbon layer, thus requiring a lower activation energy to form the *COOH intermediate compared to that of individual NiN_4 active sites.

2. Experimental

2.1 Materials and reagents

Single-walled carbon nanotubes (SWNTs, length 1–5 μm) were purchased from Nanjing XFNANO Materials Tech Co., Ltd., and formamide and potassium bicarbonate ($KHCO_3$) were provided by Macklin Biochemical Co., Ltd. Anhydrous ethanol (EtOH) and *N,N*-dimethylformamide (DMF) were obtained from Meryer Co., Ltd. All other reagents were used directly and without any treatment.

2.2 Synthesis of polyformamide decorated SWNTs (PFA@SWNTs)

Typically, 100 mg of commercial SWNTs were initially dispersed in 30 mL of formamide solvent under sonication for 0.5 h to form a homogeneous solution. Then the SWNT suspension was transferred into a 100 mL Teflon-lined autoclave, sealed and heated at 180 °C for 12 h. The obtained PFA@SWNTs black product was centrifuged and purified with deionized water and ethanol 3 times, and dried at 100 °C overnight for further use.

2.3 Synthesis of Ni partially atomized SWNTs (f-SWNTs-*T*)

The obtained PFA@SWNTs powder was transferred into a porcelain boat and heated in a tube furnace at different temperatures ($T = 600, 650, 700$ °C) for 3 h with a ramp rate of 5 °C min^{-1} under a flowing Ar atmosphere. During the process, the PFA was carbonized and converted into N-doped carbon while partial Ni NPs were thermally atomized to generate NiN_x moieties, thus obtaining the f-SWNTs-*T* catalysts.

2.4 Characterization

Transmission electron microscopy (TEM) was carried out using an FEI Tecnai G2 F20S-Twin microscope at an accelerating voltage of 200 kV. The samples were ultrasonically dispersed in ethanol, and a drop of this dispersion was placed on a microgrid for imaging. Nickel loading was quantified using a NexION 350X inductively coupled plasma mass spectrometer (ICP-MS). Liquid products were characterized by proton nuclear magnetic resonance (^1H NMR) spectroscopy, with water peak suppression achieved *via* solvent presaturation. X-ray diffraction (XRD) analysis was performed on a Rigaku Ultima IV diffractometer with Cu-Kα radiation, scanning across a 2θ range of 10–80°. X-ray photoelectron spectroscopy (XPS) measurements were conducted using a PHI-5702 system, with the C 1s peak at 284.5 eV as the binding energy reference. Nitrogen adsorption–desorption isotherms were measured using an ASAP2020 analyzer. Prior to analysis, all samples were degassed under vacuum at 393 K for 6 hours. The surface area was calculated using the Brunauer–Emmett–Teller (BET) method, while the pore volume and size distribution were determined using the Barrett–Joyner–Halenda (BJH) model. Raman spectra were obtained using a confocal Raman spectrometer (iHR-550, Horiba) with a 532 nm excitation laser. Fourier transform infrared (FT-IR) spectra were recorded using a Nicolet iS5 spectrophotometer with KBr pellets. X-ray absorption fine structure (XAFS) spectroscopy was conducted at the 1W2B beamline of the Beijing Synchrotron Radiation Facility.

3. Results and discussion

3.1 Synthesis and characterization of the f-SWNTs-*T* catalysts

The synthesis procedure of the f-SWNTs-650 catalyst is shown in Scheme 1. First, formamide was *in situ* self-condensed by a Schiff base reaction to form chain polyformamide (PFA) and attached to the surface of pristine SWNTs.[27] Second, the PFA@SWNTs hybrid was placed in a tube furnace and subjected to thermal activation treatment in an Ar atmosphere. During
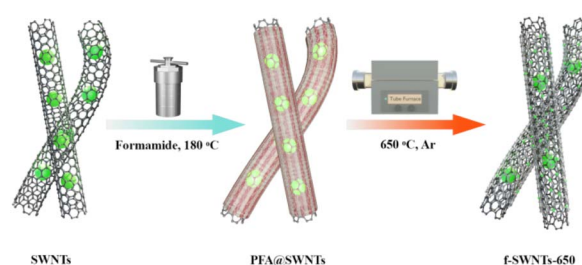
Scheme 1 Schematic illustration of the synthesis of the f-SWNTs-650 catalyst.

the process, the bulky Ni NPs were partially atomized to form Ni single atoms,[28] while those unatomized Ni NPs remained in the target catalyst structure.[29] The Ni NPs encapsulated in the carbon layer inject electrons into the Ni single atoms within conductive SWNT matrices, thereby serving as a co-catalyst to enhance the catalytic performance of the Ni single atom sites for the CO_2RR.[30]

As shown in Fig. 1a, the transmission electron microscopy (TEM) image reveals that the commercial SWNTs prepared by the arc discharge method are stacked in bundles of nanotubes,[31–34] and there are a large number of Ni NPs with a diameter range from 5 to 20 nm. The high-resolution TEM image shows that there is still a portion of amorphous carbon on the SWNT surface and these Ni NPs are gathered around them (Fig. 1b). The result of inductively coupled plasma mass spectrometry (ICP-MS) shows that the residual Ni content in SWNTs is as high as 25.2 wt%, which provides unique conditions for their subsequent functionalization and utilization.[35–37] Interestingly, a portion of bulk Ni NPs disappear in the PFA@SWNTs sample after mild heat treatment in an Ar atmosphere (Fig. 1c and d). The Ni loading in the f-SWNTs-650 catalyst is found be reduced to 15.2 wt% by ICP-MS analysis, which is consistent with the TEM result. The spherical aberration-corrected high-angle annular dark field scanning transmission electron microscopy (HAADF-STEM) distinctly reveals numerous bright spots on the f-SWNTs-650 catalyst surface, in addition to Ni NPs of varying sizes, demonstrating that the isolated Ni sites are successfully anchored on the surface of SWNTs (Fig. 1e–g and S1†).[38] Energy dispersive X-ray spectroscopy (EDS) images illustrate the uniform distribution of C, N, O, and Ni elements within the f-SWNTs-650 sample (Fig. 1h). The above results indicate that the residual Ni NPs in pristine SWNTs undergo a partial thermal atomization process after such specific post-treatment.

X-ray diffraction (XRD) patterns of SWNTs and f-SWNTs-T (T = 600, 650 and 700 °C) confirm that besides the C (002) and C (101) graphitic carbon peaks of SWNTs at 26.6° and 44.0°, additional Ni (111), Ni (200) and Ni (220) diffraction peaks also appear at 45.0°, 52.3° and 76.8°,[39,40] proving the presence of Ni NPs in SWNTs before and after heat treatment (Fig. S2†), which is in agreement with the TEM results. The Raman spectra of all samples are shown in Fig. S3.† The spectrum of SWNTs displays moderately split G-bands. The G band is divided into two degenerate modes (1551.4 cm^{-1} G_- and 1577.3 cm^{-1} G_+) by the curvature of SWNTs.[41] In contrast, the G_+ and G_- bands of f-SWNTs-T catalysts exhibit upshift displacements of 12.4 and 9.8 cm^{-1} due to the charge transfer induced interactions between SWNTs and encapsulated Ni NPs.[37] N_2 adsorption–desorption analysis was conducted to determine the textural properties of the pristine SWNTs and the as-prepared f-SWNTs-T catalysts (Fig. S4 and Table S1†). The pristine SWNTs exhibit weak adsorption of N_2 before P/P_0 = 0.9, followed by upward adsorption, suggesting a type-III isotherm with a surface area of 283.1 m^2 g^{-1}. After surface modification and mild heat treatment, the surface area of the f-SWNTs-650 catalyst increases to 358.9 m^2 g^{-1} and the pore volume increases from 1.33 to 2.09 m^3 g^{-1} compared to the pristine SWNTs. Such a high surface area facilitates the high accessibility of Ni single atoms and the adsorption and activation of CO_2 molecules during the CO_2RR process.[42,43] Fourier transform infrared (FTIR) spectra show that the main functional groups of C–N (1388 cm^{-1}) and C=N (1627 cm^{-1}) are present in the PFA skeleton, suggesting the successful condensation of FA via the solvothermal method. However, both C–O–C (1389 cm^{-1}) and C=C (1632 cm^{-1}) groups in SWNTs and f-SWNTs-T catalysts appear at frequencies close to the absorption bands of PFA, making it difficult to distinguish these functional groups (Fig. S5†).[44]
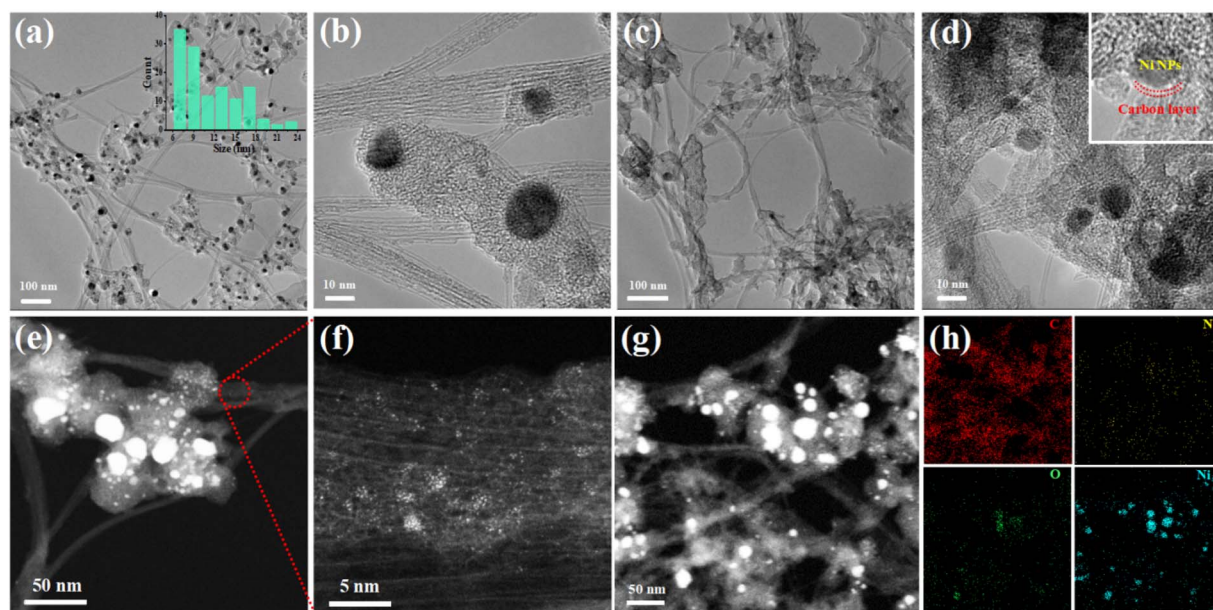

Fig. 1 (a and b) TEM and HRTEM images of initial SWNTs, (c and d) TEM and HRTEM images of the f-SWNTs-650 catalyst, (e and f) high-resolution HAADF-STEM and (g and h) HAADF-STEM and the corresponding EDS images of the f-SWNTs-650 catalyst.

X-ray absorption near edge structure (XANES) and extended X-ray absorption fine structure (EXAFS) analyses of the Ni K-edge were conducted to elucidate the local coordination environment,[45,46] bonding mode, and valence state of the SWNTs and f-SWNTs-650 catalyst. As shown in Fig. 2a, the Ni absorption edge position of pristine SWNTs is slightly lower than that of the Ni foil, indicating that Ni obtains electrons from SWNTs and is present in a metallic state.[47] The absorption edge position of f-SWNTs-650 is between Ni foil and NiO, suggesting that the average valence of Ni species is at a partially oxidized state.[48,49] Considering that the valence state of Ni NPs is zero, the higher oxidation state implies the existence of another coordination mode of atomically dispersed Ni species in the f-SWNTs-650 catalyst. Fourier transformed Ni K-edge extended XAFS spectra (EXAFS) display two major peaks at 1.45 Å and 2.19 Å for f-SWNTs-650, which are attributed to the Ni–N and Ni–Ni scattering paths, respectively (Fig. 2b).[50] Compared with the pristine SWNTs, the intensity of the Ni–Ni peak is reduced and accompanied by the appearance of the Ni–N peak for the f-SWNTs-650 catalyst, indicating that the low-temperature heat treatment triggers partial thermal atomization of residual Ni NPs in SWNTs. To further quantify the coordination environment of the Ni species, curve fitting of EXAFS spectra was conducted.[51] The fitting result in Fig. 2c proves that the average coordination number of Ni is determined to be 3.7, which is consistent with a NiN_4 configuration (Table S2†). The wavelet transform (WT) plot of f-SWNTs-650 shows that in addition to the maximum intensity of Ni–Ni coordination at 6.8 Å^{-1} compared with Ni foil,[52] a trailing peak appears at 4–6 Å^{-1}, which is ascribed to Ni–N coordination,[53] further revealing the coexistence of NiN_4 and Ni NPs in such a catalyst (Fig. 2d–f).

3.2 Evaluation of the CO_2RR performance of f-SWNTs-T catalysts

The CO_2 electroreduction performance of the pristine SWNTs and f-SWNTs-T (T = 600, 650 and 700 °C) catalysts was investigated in an H-type electrolytic cell saturated with high-purity CO_2 using 0.5 M $KHCO_3$. The linear sweep voltammetry (LSV) curves display an enhanced cathodic current density and a more positive shift in onset potential in a CO_2 protected atmosphere than that of the N_2 saturated solution (Fig. S6†). As shown in Fig. 3a, the LSV curve of the pristine SWNTs shows a low cathode current density, suggesting that the SWNTs have unobvious catalytic activity against the CO_2RR, while the f-SWNTs-T catalyst presents a high cathode current density, indicative of the excellent catalytic capacity for the CO_2RR. Then, steady-state electrolysis was performed in the potential range of −0.52 V to −1.22 V vs. RHE to detect the changes in selectivity and catalytic activity of these catalysts. The gas and liquid products were analyzed by gas chromatography (GC) and ^1H nuclear magnetic resonance (^1H NMR),[54] respectively. As shown in Fig. 3b and S7,† the FE_{CO} values of initial SWNTs and PFA@SWNTs are consistently less than 5.4% throughout the entire potential window, proving that these Ni NPs only play a role in the HER and have negligible activity for the CO_2RR to CO. Unexpectedly, the FE_{CO} of the f-SWNTs-T (T = 600, 650 and 700 °C) catalysts is always higher than 92.4% in the potential range of −0.72 to −1.02 V vs. RHE, which is in sharp contrast to pristine SWNTs. Especially for the f-SWNTs-650 catalyst, the FE_{CO} reaches 97.9% and the partial current density of CO (j_{CO}) is −15.6 mA cm^{-2} at −0.92 V vs. RHE (Fig. 3c), which exceeds those of the most advanced electrocatalysts across a broad
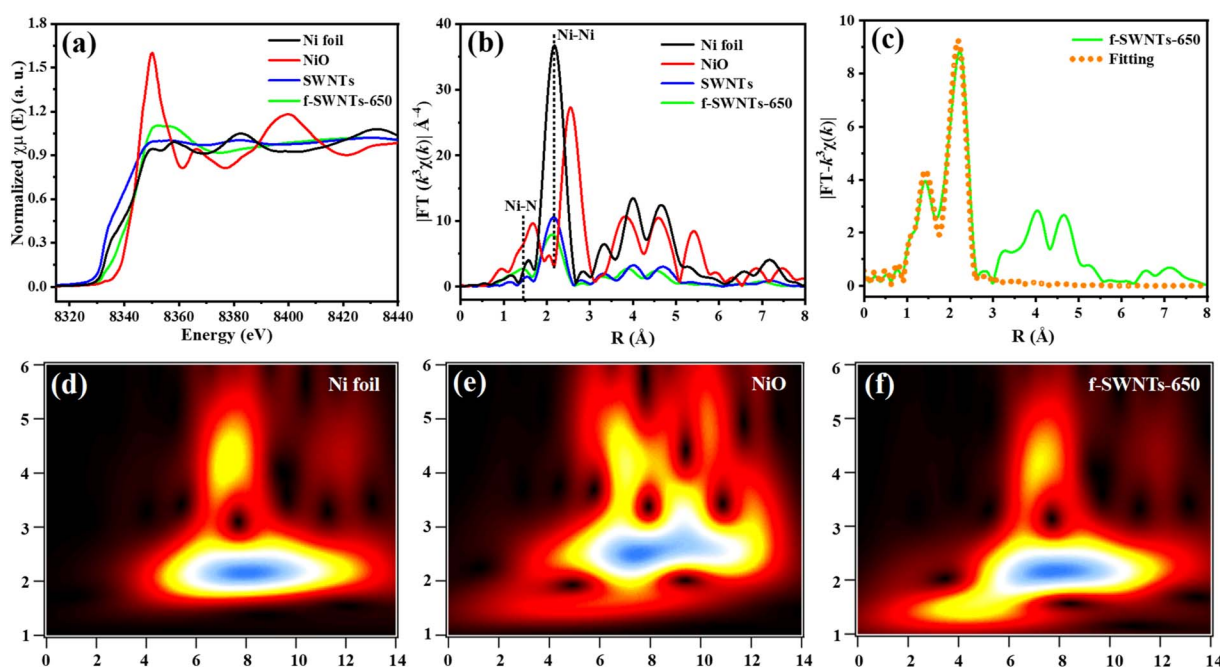

Fig. 2 (a) XANES spectra at the Ni K-edge, (b) Fourier transformed (FT) k^3-weighted $\chi(k)$-function of the EXAFS spectra for Ni foil, NiO, SWNTs and f-SWNTs-650, (c) EXAFS fitting curves of the f-SWNTs-650 catalyst at R space (inset showing the schematic model) and (d–f) WT for the k^3-weighted EXAFS signals of Ni foil, NiO and the f-SWNTs-650 catalyst.
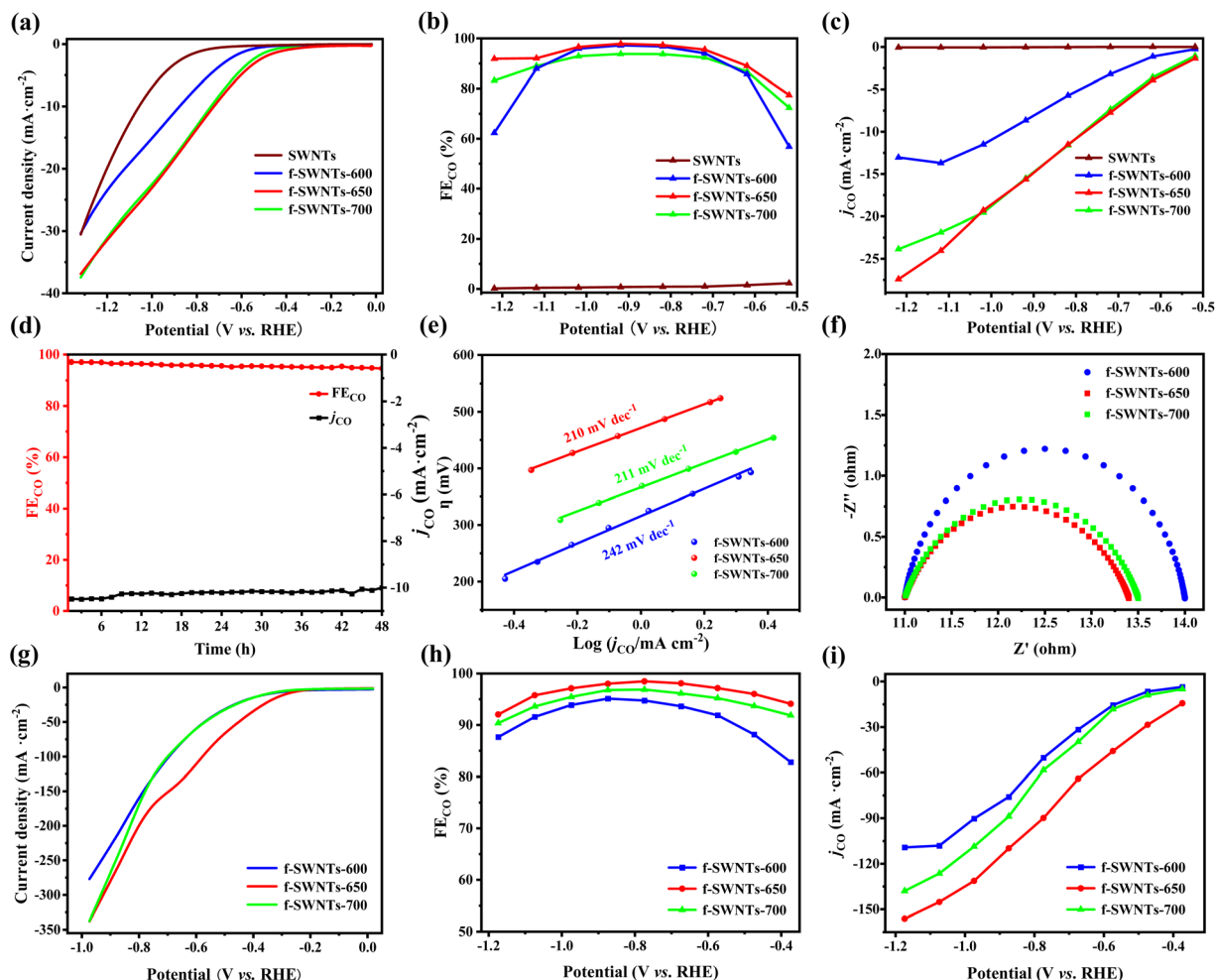
Fig. 3 In the H-type electrolytic cell: (a) linear sweep voltammetry curves, (b) FE_{CO} and (c) CO partial current density at different potentials, (d) long-term stability of the f-SWNTs-650 catalyst at −0.82 V $vs.$ RHE, (e) Tafel slope, and (f) Nyquist plots. In the flow cell: (g) linear sweep voltammetry curves, (h) FE_{CO} and (i) CO partial current density at different potentials.

spectrum of potentials in H-type cells (Table S3†). Therefore, an appropriate thermal atomization temperature is crucial for the equilibrium relationship between Ni single atoms and Ni NPs, as well as the overall performance of CO_2 electroreduction. As shown in Fig. S8,† no liquid products are detected, indicating that CO is the only product in the CO_2RR process. The electrochemical stability is a pivotal criterion to evaluate the catalyst performance in the CO_2RR. The long-term durability of the f-SWNTs-650 catalyst has been evaluated at −0.82 V $vs.$ RHE for the CO_2RR, and it is found that the FE_{CO} and j_{CO} are 95.0% and −10.0 mA cm^{-2} and the catalyst maintains excellent stability throughout the 48 h potentiostatic electrolysis period (Fig. 3d). The linear fitting result between the logarithm of partial current density (j_{CO}) and overpotential (η) shows that the Tafel slopes of f-SWNTs-600, f-SWNTs-650 and f-SWNTs-700 catalysts are 210, 211 and 242 mV dec^{-1}, indicating that the first protonation of CO_2 to form the *COOH intermediate is the rate-determining step and f-SWNTs-650 has the highest catalytic reactivity (Fig. 3e). Electrochemical impedance spectra (EIS) reveal that f-SWNTs-650 possesses the lowest faradaic impedance compared

to the other two catalysts, indicating that the charge transfer rate of the f-SWNTs-650 catalyst is the highest during the reaction (Fig. 3f), consistent with the electrocatalytic performance of the CO_2RR.

To assess the performance of the catalysts at industrial current densities, we further evaluated the CO_2RR performance in flow cells using gas diffusion electrodes (GDEs). Fig. 3g shows the LSV curves of f-SWNTs-600, f-SWNTs-650, and f-SWNTs-700. Using 1.0 M KOH as the anolyte and catholyte, the f-SWNTs-650 catalyst outperforms both f-SWNTs-600 and f-SWNTs-700. As shown in Fig. 3h, the FE_{CO} of the f-SWNTs-600, f-SWNTs-650 and f-SWNTs-700 catalysts can reach 94.7%, 98.5%, and 97.8% at −0.77 V $vs.$ RHE, respectively. Similarly, in Fig. 3i, the j_{CO} of f-SWNTs-600, f-SWNTs-650 and f-SWNTs-700 can reach −109.3 mA cm^{-2}, −156.2 mA cm^{-2} and −138.0 mA cm^{-2} at −1.17 V $vs.$ RHE. Respectively, it is noteworthy that the f-SWNTs-650 catalyst can maintain an FE_{CO} of 92.0% at −1.17 V $vs.$ RHE. Comparing the performance of the catalysts in the H-cell and the flow cell shows similar results, with the f-SWNTs-650 catalyst exhibiting the best performance.

3.3 The possible mechanism of the CO₂RR on the f-SWNTs-650 catalyst

To gain insight into the surface valence state and composition evolution of metal Ni species, X-ray photoelectron spectroscopy (XPS) was performed on the pristine SWNTs and f-SWNTs-650 samples.[55] The full-survey XPS spectrum of f-SWNTs-650 proves the coexistence of Ni, C, N and O elements (Fig. S9†), which is in good agreement with the EDS mapping analyses. The deconvoluted high-resolution XPS N 1s spectrum of f-SWNTs-650 exhibits five typical peaks at 398.3, 399.1, 400.1, 401.3 and 404.4 eV, which are attributed to pyridinic-N, Ni–N, pyrrolic-N, graphitic-N and oxidized N, respectively (Fig. 4a). In Fig. 4b, the Ni 2p binding energy of the SWNTs is determined to be 852.8 eV, corresponding to the Ni $2p_{3/2}$ signals of Ni (0),[56] while the binding energy at 856.1 eV is ascribed to the partial oxidation of the Ni NPs. Combined with the CO₂RR test results, it can be seen that the residual Ni NPs on the pristine SWNTs only play a role in the hydrogen evolution reaction (HER) and hardly produce any CO. In contrast, the fitting results show that the binding energy of Ni $2p_{3/2}$ in the f-SWNTs-650 catalyst has a dominant peak at 855.8 eV, which is close to that of Ni $2p_{3/2}$ in NiPc (855.4 eV) except for the binding energy of Ni (0) at 853.0 eV.[57] The results confirm that the residual Ni NPs on pristine SWNTs can be thermally atomized into Ni single atoms through formamide polymerisation combined with mild heat treatment. The FE_CO of f-SWNTs-650 dramatically increases from 0.8% to 97.9% at −0.82 V vs. RHE compared to that of the pristine SWNTs, indicating that the thermally atomized Ni sites play a decisive role in the CO₂RR. Moreover, the binding energy of Ni (0) at Ni $2p_{3/2}$ in the f-SWNTs-650 catalyst is positively shifted by

0.2 eV compared with that of the pristine SWNTs, indicating that the electrons transfer from Ni NPs to Ni single atoms, which is related to the synergistic interaction between them.

To investigate the origin of the significantly improved catalytic performance of the CO₂RR to CO on the f-SWNTs-650 catalyst, density functional theory (DFT) calculations were carried out. Herein, the Ni single atom coordinated with four N atoms embedded in graphene (NiN₄), and the NiN₄ site combined with face-centered cubic Ni (111) (NiN₄ & Ni NPs) were regarded as the targeted structure according to the XAFS, XPS and XRD results (Fig. S10†). Generally, the *COOH and *CO are viewed as the first and second reaction intermediates for electrochemical CO₂-to-CO conversion. The charge density differences of NiN₄ & Ni NPs were calculated. It was shown that the electrons of Ni NPs were significantly transferred to the NiN₄ site (Fig. 4c and d). As shown in Fig. 4e, the free energy for *COOH formation is 1.01 eV and 0.83 eV for NiN₄ and NiN₄ & Ni NPs sites, demonstrating that the introduction of Ni NPs into the NiN₄ structure reduces the activation energy barrier of CO₂ and promotes the electrocatalytic activity of the f-SWNTs-650 electrocatalyst. The subsequent *CO formation is an exothermic reaction for both structures, which is a thermodynamically favorable process. Thus, the formation of the *COOH intermediate is the rate-limiting step for the CO₂RR, which is consistent with the previous reports.[18] In addition, Zhao's group has demonstrated that the Ni NPs can inject additional electrons into the NiN₃ structure through the carbon layer to reduce the free energy of the *COOH, which is conducive to the smooth progress of the CO₂RR.[58] We also calculated the total density of states (DOS) of NiN₄ and NiN₄ & Ni NPs. The density of states at
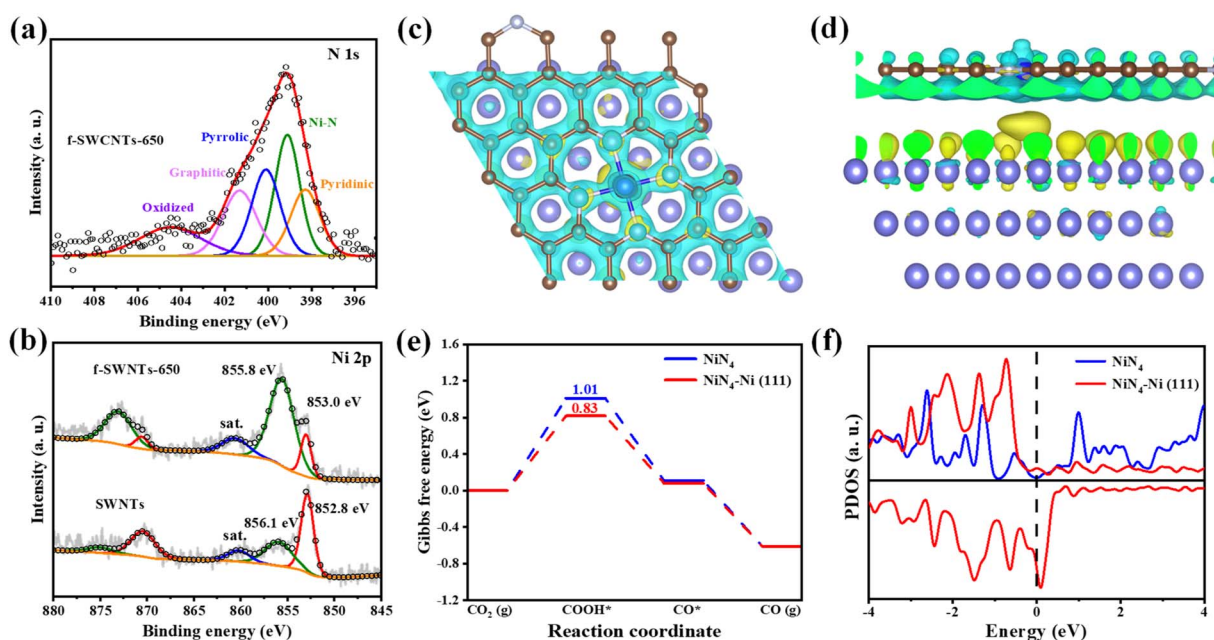

Fig. 4 (a) High-resolution XPS N 1s spectrum of the f-SWNTs-650 catalyst, (b) high-resolution XPS spectra analysis in the Ni 2p region of SWNTs and the f-SWNTs-650 catalyst, (c and d) charge density difference for the NiN₄−Ni (111) active site (top and side view), (e) free-energy diagrams for the CO₂RR to CO over NiN₄ and NiN₄−Ni (111) active sites and (f) the density of states (DOS) of the d orbitals of Ni atoms on NiN₄ and NiN₄−Ni (111) (the dotted black line indicates the Fermi level).

the Fermi level is higher on NiN$_4$ & Ni NP active sites compared to the bare NiN$_4$ site, which favours the electrocatalytic process (Fig. 4f). Therefore, the DFT calculations indicate that the NiN$_4$ & Ni NP sites play a crucial role in the enhanced catalytic activity of the f-SWNTs-650 catalyst.

4. Conclusion

In summary, a high-performance f-SWNTs-650 catalyst with highly accessible NiN$_4$ sites decorated with Ni NPs was prepared by a simple solvothermal reaction and a mild heat treatment. The thermal atomization strategy is effective in partially converting residual Ni particles into atomically dispersed NiN$_4$ species over the commercial SWNT matrices. The catalyst exhibited 97.9% of FE$_{CO}$, -15.6 mA cm^{-2} of j_{CO} at -0.92 V *vs.* RHE, and FE$_{CO}$ > 96% over a wide potential window (-0.72 V to -1.02 V), achieving a significant improvement of the catalytic performance in comparison with that of the pristine SWNTs for the CO$_2$RR. The excellent CO$_2$-to-CO conversion performance can be attributed to the partial atomization of residual Ni NPs on SWNTs to generate new NiN$_4$ active sites by low temperature heat treatment. Detailed characterization and DFT calculations demonstrate that the presence of Ni NPs significantly enhances the CO$_2$ activation capability of NiN$_4$–Ni sites by injecting additional electrons, which requires a lower activation energy to form the *COOH intermediate compared to the individual NiN$_4$ site. The present work provides a new approach for preparing high-performance CO$_2$RR catalysts starting directly from commercialized SWNTs under mild conditions, which are superior to other supported metal phthalocyanine/porphyrin molecular catalysts and their derived M–N–C catalysts prepared by high-temperature pyrolysis. Therefore, the partial thermal atomization approach proposed in this work not only provides new insights into efficient synergistic catalysis between metal single atoms and nanoparticles, but also offers new catalytic systems for important energy and environmental-related catalytic reactions.

Data availability

The electron microscopy images, characterization data and electrochemical data can be found in the ESI.†

Author contributions

F. Zhang: writing the original draft, investigation. H. Zhang: data curation, formal analysis. Y. Zhao: data curation, formal analysis. J. Li: conceptualization, methodology. C. Guan: data curation, software. J. Li: investigation, formal analysis. X. Wang: formal analysis, validation. Y. Mu: software, methodology. W.-Y. Zan: software, funding acquisition. S. Zhu: review & editing, supervision, project administration.

Conflicts of interest

There are no conflicts to declare.

Acknowledgements

Notes and references

1 X. Chang, T. Wang, P. Yang, G. Zhang and J. Gong, *Adv. Mater.*, 2019, **31**, 1804710.

2 E. Nikoloudakis, I. López-Duarte, G. Charalambidis, K. Ladomenou, M. Ince and A. G. Coutsolelos, *Chem. Soc. Rev.*, 2022, **51**, 6965–7045.

3 X. Jie, S. Gonzalez-Cortes, T. Xiao, B. Yao, J. Wang, D. R. Slocombe, Y. Fang, N. Miller, H. A. Al-Megren, J. R. Dilworth, J. M. Thomas and P. P. Edwards, *Energy Environ. Sci.*, 2019, **12**, 238–249.

4 P. Tyagi, D. Singh, N. Malik, S. Kumar and R. S. Malik, *Mater. Today*, 2023, **65**, 133–165.

5 J. Xiao, G. He, S. Fan and Z. Li, *Appl. Energy*, 2022, **328**, 120219.

6 C. Zhang, Y. Yang, X. Liu, M. Mao, K. Li, Q. Li, G. Zhang and C. Wang, *Innovation*, 2023, **4**, 100518.

7 B. Pickering, F. Lombardi and S. Pfenninger, *Joule*, 2022, **6**, 1253–1276.

8 P. Sun, S. Liu, X. Zheng, G. Hu, Q. Zhang, X. Liu, G. Zheng and Y. Chen, *Nano Today*, 2024, **55**, 102152.

9 K. Kamada, J. Jung, C. Yamada, T. Wakabayashi, K. Sekizawa, S. Sato, T. Morikawa, S. Fukuzumi and S. Saito, *Angew. Chem., Int. Ed.*, 2024, e202403886.

10 M. Wang, B. Wang, J. Zhang, S. Xi, N. Ling, Z. Mi, Q. Yang, M. Zhang, W. R. Leow, J. Zhang and Y. Lum, *Nat. Commun.*, 2024, **15**, 1218.

11 S. Zhang, Q. Fan, R. Xia and T. J. Meyer, *Acc. Chem. Res.*, 2020, **53**, 255–264.

12 Z. Zhang, M. Li, R. Gao, S. Yang, Q. Ma, R. Feng, H. Dou, J. Dang, G. Wen, Z. Bai, D. Liu, M. Feng and Z. Chen, *J. Am. Chem. Soc.*, 2024, **146**, 6397–6407.

13 A. Bairagi, A. Y. Pereverzev, P. Tinnemans, E. A. Pidko and J. Roithová, *J. Am. Chem. Soc.*, 2024, **146**, 5480–5492.

14 T. Yan, X. Chen, L. Kumari, J. Lin, M. Li, Q. Fan, H. Chi, T. J. Meyer, S. Zhang and X. Ma, *Chem. Rev.*, 2023, **123**, 10530–10583.

15 S. Cao, S. Zhou, H. Chen, S. Wei, S. Liu, X. Lin, X. Chen, Z. Wang, W. Guo and X. Lu, *Energy Environ. Mater.*, 2023, **6**, e12287.

16 G. Liu, G. Yang, X. Peng, J. Wu and N. Tsubaki, *Chem. Soc. Rev.*, 2022, **51**, 5606–5659.

17 S. Liang, L. Huang, Y. Gao, Q. Wang and B. Liu, *Adv. Sci.*, 2021, **8**, 2102886.

18 S. Jin, Z. Hao, K. Zhang, Z. Yan and J. Chen, *Angew. Chem., Int. Ed.*, 2021, **60**, 20627–20648.

19 S. Vijay, W. Ju, S. Brückner, S.-C. Tsang, P. Strasser and K. Chan, *Nat. Catal.*, 2021, **4**, 1024–1031.

20 Y. Zhu, X. Cui, H. Liu, Z. Guo, Y. Dang, Z. Fan, Z. Zhang and W. Hu, *Nano Res.*, 2021, **14**, 4471–4486.

21 E. Zhang, T. Wang, K. Yu, J. Liu, W. Chen, A. Li, H. Rong, R. Lin, S. Ji, X. Zheng, Y. Wang, L. Zheng, C. Chen, D. Wang, J. Zhang and Y. Li, *J. Am. Chem. Soc.*, 2019, **141**, 16569–16573.

22 S. Lyu, H. Chang, L. Zhang, S. Wang, S. Li, Y. Lu and S. Li, *Composites, Part B*, 2023, **264**, 110888.

23 Y. Zhu, L. Li, C. Zhang, G. Casillas, Z. Sun, Z. Yan, G. Ruan, Z. Peng, A.-R. O. Raji, C. Kittrell, R. H. Hauge and J. M. Tour, *Nat. Commun.*, 2012, **3**, 1225.

24 X. Shi, B. Sitharaman, Q. P. Pham, F. Liang, K. Wu, W. E. Billups, L. J. Wilson and A. G. Mikos, *Biomaterials*, 2007, **28**, 4078–4090.

25 L. A. Montoro, C. A. Luengo, J. M. Rosolen, E. Cazzanelli and G. Mariotto, *Diamond Relat. Mater.*, 2003, **12**, 846–850.

26 H. Zhang, Y. Liu, L. Cao, D. Wei, Y. Wang, H. Kajiura, Y. Li, K. Noda, G. Luo, L. Wang, J. Zhou, J. Lu and Z. Gao, *Adv. Mater.*, 2009, **21**, 813–816.

27 G. Zhang, Y. Jia, C. Zhang, X. Xiong, K. Sun, R. Chen, W. Chen, Y. Kuang, L. Zheng, H. Tang, W. Liu, J. Liu, X. Sun, W.-F. Lin and H. Dai, *Energy Environ. Sci.*, 2019, **12**, 1317–1325.

28 Q. Fan, P. Hou, C. Choi, T.-S. Wu, S. Hong, F. Li, Y.-L. Soo, P. Kang, Y. Jung and Z. Sun, *Adv. Energy Mater.*, 2020, **10**, 1903068.

29 L. Zhang, D.-M. Sun, P.-X. Hou, C. Liu, T. Liu, J. Wen, N. Tang, J. Luan, C. Shi, J.-C. Li, H.-T. Cong and H.-M. Cheng, *Adv. Mater.*, 2017, **29**, 1605719.

30 Y. He, Y. Li, J. Zhang, S. Wang, D. Huang, G. Yang, X. Yi, H. Lin, X. Han, W. Hu, Y. Deng and J. Ye, *Nano Energy*, 2020, **77**, 105010.

31 T. Cui, X. Pan, J. Dong, S. Miao, D. Miao and X. Bao, *Nano Res.*, 2018, **11**, 3132–3144.

32 H. Huang, J. Marie, H. Kajiura and M. Ata, *Nano Lett.*, 2002, **2**, 1117–1119.

33 L. A. Montoro and J. M. Rosolen, *Carbon*, 2006, **44**, 3293–3301.

34 R. Fleurier, J.-S. Lauret, U. Lopez and A. Loiseau, *Adv. Funct. Mater.*, 2009, **19**, 2219–2223.

35 G. Başkaya, Y. Yıldız, A. Savk, T. O. Okyay, S. Eriş, H. Sert and F. Şen, *Biosens. Bioelectron.*, 2017, **91**, 728–733.

36 Y.-S. Lo, D. H. Nam, H.-M. So, H. Chang, J.-J. Kim, Y. H. Kim and J.-O. Lee, *ACS Nano*, 2009, **3**, 3649–3655.

37 S. Zhu, L. Ding, X. Zhang, K. Wang, X. Wang, F. Yang and G. Han, *Angew. Chem., Int. Ed.*, 2023, **62**, e202309545.

38 T. Zhang, X. Han, H. Yang, A. Han, E. Hu, Y. Li, X.-q. Yang, L. Wang, J. Liu and B. Liu, *Angew. Chem., Int. Ed.*, 2020, **59**, 12055–12061.

39 N. Wei, Y. Tian, Y. Liao, N. Komatsu, W. Gao, A. Lyuleeva-Husemann, Q. Zhang, A. Hussain, E.-X. Ding, F. Yao, J. Halme, K. Liu, J. Kono, H. Jiang and E. I. Kauppinen, *Adv. Mater.*, 2021, **33**, 2170060.

40 W. Ni, T. Wang, F. Héroguel, A. Krammer, S. Lee, L. Yao, A. Schüler, J. S. Luterbacher, Y. Yan and X. Hu, *Nat. Mater.*, 2022, **21**, 804–810.

41 C.-C. Chang, C.-C. Chen, W.-H. Hung, I. K. Hsu, M. A. Pimenta and S. B. Cronin, *Nano Res.*, 2012, **5**, 854–862.

42 F. Zhang, H. Zhang, Z. Jia, S. Chen, S. Li, J. Li, W.-Y. Zan, Q. Wang and Y. Li, *Small*, 2023, **20**, 2308080.

43 G. Li, Y. Qin, Y. Wu, L. Pei, Q. Hu, H. Yang, Q. Zhang, J. Liu and C. He, *Chin. J. Catal.*, 2020, **41**, 830–838.

44 L. Liu, L. Lei, K. Zeng, K. Wu and N. Yang, *Adv. Funct. Mater.*, 2023, **33**, 2211335.

45 K. Jiang, S. Siahrostami, T. Zheng, Y. Hu, S. Hwang, E. Stavitski, Y. Peng, J. Dynes, M. Gangisetty, D. Su, K. Attenkofer and H. Wang, *Energy Environ. Sci.*, 2018, **11**, 893–903.

46 D. Qiu, W. Zhao, B. Zhang, M. T. Ahsan, Y. Wang, L. Zhang, X. Yang and Y. Hou, *Adv. Energy Mater.*, 2024, 2400002.

47 J. Yang, Z. Qiu, C. Zhao, W. Wei, W. Chen, Z. Li, Y. Qu, J. Dong, J. Luo, Z. Li and Y. Wu, *Angew. Chem., Int. Ed.*, 2018, **57**, 14095–14100.

48 S. Zhou, Y. Zhao, R. Shi, Y. Wang, A. Ashok, F. Héraly, T. Zhang and J. Yuan, *Adv. Mater.*, 2022, **34**, 2204388.

49 F. Zhang, J. Li, Y. Chen, H. Zhang, J. Li, P. Liu, Y. Mu, W.-Y. Zan and Z. Sun, *J. Catal.*, 2024, **433**, 115495.

50 T. Ding, X. Liu, Z. Tao, T. Liu, T. Chen, W. Zhang, X. Shen, D. Liu, S. Wang, B. Pang, D. Wu, L. Cao, L. Wang, T. Liu, Y. Li, H. Sheng, M. Zhu and T. Yao, *J. Am. Chem. Soc.*, 2021, **143**, 11317–11324.

51 J. Chen, D. Wang, X. Yang, W. Cui, X. Sang, Z. Zhao, L. Wang, Z. Li, B. Yang, L. Lei, J. Zheng, L. Dai and Y. Hou, *Angew. Chem., Int. Ed.*, 2023, **62**, e202215406.

52 M. Hou, L. Zheng, D. Zhao, X. Tan, W. Feng, J. Fu, T. Wei, M. Cao, J. Zhang and C. Chen, *Nat. Commun.*, 2024, **15**, 1342.

53 C. Xia, Y. Qiu, Y. Xia, P. Zhu, G. King, X. Zhang, Z. Wu, J. Y. Kim, D. A. Cullen, D. Zheng, P. Li, M. Shakouri, E. Heredia, P. Cui, H. N. Alshareef, Y. Hu and H. Wang, *Nat. Chem.*, 2021, **13**, 887–894.

54 H. Guo, D.-H. Si, H.-J. Zhu, Z.-A. Chen, R. Cao and Y.-B. Huang, *Angew. Chem., Int. Ed.*, 2024, **63**, e202319472.

55 L. Jiao, J. Zhu, Y. Zhang, W. Yang, S. Zhou, A. Li, C. Xie, X. Zheng, W. Zhou, S.-H. Yu and H.-L. Jiang, *J. Am. Chem. Soc.*, 2021, **143**, 19417–19424.

56 X. Weng, M. Guo, F. Luo and Z. Chen, *Chem. Eng. J.*, 2017, **308**, 904–911.

57 R. Yao, K. Sun, K. Zhang, Y. Wu, Y. Du, Q. Zhao, G. Liu, C. Chen, Y. Sun and J. Li, *Nat. Commun.*, 2024, **15**, 2218.

58 W. Ren, X. Tan, C. Jia, A. Krammer, Q. Sun, J. Qu, S. C. Smith, A. Schueler, X. Hu and C. Zhao, *Angew. Chem., Int. Ed.*, 2022, **61**, e202203335.